Genesis and growth of extracellular vesicle-derived microcalcification in atherosclerotic plaques

Published in final edited form as:

Nat Mater. 2016 March ; 15(3): 335–343. doi:10.1038/nmat4519.

Genesis and growth of extracellular vesicle-derived microcalcification in atherosclerotic plaques

Joshua D. Hutcheson[1], **Claudia Goettsch**[1], **Sergio Bertazzo**[2], **Natalia Maldonado**[1], **Jessica L. Ruiz**[1], **Wilson Goh**[1], **Katsumi Yabusaki**[1], **Tyler Faits**[1], **Carlijn Bouten**[3], **Gregory Franck**[4], **Thibaut Quillard**[4], **Peter Libby**[4], **Masanori Aikawa**[1,4], **Sheldon Weinbaum**[5], and **Elena Aikawa**[1,4]

[1]Center for Interdisciplinary Cardiovascular Sciences, Cardiovascular Medicine, Brigham and Women's Hospital, Harvard Medical School, Boston, MA, USA [2]Department of Medical Physics & Biomedical Engineering, University College London, London, UK [3]Department of Biomedical Engineering, Eindhoven University of Technology, Eindhoven, The Netherlands [4]Center for Excellence in Vascular Biology, Brigham and Women's Hospital, Harvard Medical School, Boston, MA, USA [5]Department of Biomedical Engineering, City College of New York, New York, NY, USA

Abstract

Clinical evidence links arterial calcification and cardiovascular risk. Finite-element modelling of the stress distribution within atherosclerotic plaques has suggested that subcellular microcalcifications in the fibrous cap may promote material failure of the plaque, but that large calcifications can stabilize it. Yet the physicochemical mechanisms underlying such mineral formation and growth in atheromata remain unknown. Here, by using three-dimensional collagen hydrogels that mimic structural features of the atherosclerotic fibrous cap, and high-resolution microscopic and spectroscopic analyses of both the hydrogels and of calcified human plaques, we demonstrate that calcific mineral formation and maturation results from a series of events involving the aggregation of calcifying extracellular vesicles, and the formation of microcalcifications and ultimately large calcification zones. We also show that calcification morphology and the plaque's collagen content – two determinants of atherosclerotic plaque stability - are interlinked.

Corresponding author: Elena Aikawa, MD, PhD, 3 Blackfan St, CLSB, CICS, 17th floor, Brigham and Women's Hospital, Boston, MA 02115, Phone: 617-730-7755, Fax: 617-730-7791, ; Email: eaikawa@partners.org

Author Contributions

JDH designed the study, performed sample preparation, conducted experimental work, carried out data interpretation and drafted the manuscript. CG aided with study design and data interpretation. SB performed DDC-SEM and EDS experiments. NM performed μCT analysis. JLR aided with super resolution microscopy and FTIR spectroscopy. WG aided with analysis of FTIR spectroscopy. KY performed image segmentation analysis of histological images. TF performed histological tissue assessment. CB provided a custom collagen probe. GF and TQ helped obtain and analyze tissue from the MMP-13-deficient mice. PL directed the generation of the MMP-13-deficient mice and provided the human carotid specimens. CB, MA, PL, and SW provided critical review of the manuscript. EA provided the study concept, participated in study design, data interpretation and aided in manuscript development.

Calcification morphology determines plaque stability

A material failure of the collagen-poor fibrous cap contributes critically to atherosclerotic plaque rupture[1], a global leading cause of death[2]. Understanding plaque integrity can benefit from connection of cellular changes to alterations in tissue material properties. Classically, plaque vulnerability associates with low collagen content in the fibrous cap, which compromises its tensile strength[3,4]. Recent computational studies, however, highlight the presence of destabilizing microcalcifications (approximately 5 μm), smaller than the resolution limits of traditional clinical imaging modalities (currently >30 μm), in the cap of "vulnerable plaques" as a determinant of their biomechanical failure[5–7]. Indeed, coronary calcium scores predict acute cardiovascular events better than traditional risk calculators[8,9]. Plaque rupture occurs when local stresses exceed a critical threshold for material failure, compromising the structural integrity of the fibrous cap. The formation of microcalcifications causes plaque instability by promoting high stress accumulation within the cap extracellular matrix (ECM)[10], likely favouring cavitation events that occur due to the large modulus mismatch between the small, stiff microcalcifications and the surrounding hyperelastic collagen[5,6].

Prospective clinical data from the Multi-Ethnic Study of Atherosclerosis trial, which showed that the abundance of arterial calcification per arterial volume correlates inversely with cardiovascular events[11], corroborates the biomechanical model predictions linking microcalcifications with plaque rupture. These data indicate that larger calcifications may stabilize atherosclerotic plaques[12–15], whereas "spotty" calcification (>30 μm) may indicate the presence of active remodeling and clinically undetectable microcalcifications (1 μm –30 μm) that contribute to plaque destabilization[16]. Thus, the calcification morphology correlates with cardiovascular risk. Yet, mechanisms that govern the formation of microcalcifications and larger, potentially plaque-stabilizing calcifications remain unknown.

Nano-analytical electron microscopy revealed structural detail of calcific mineral within cardiovascular tissues[17]. The formation of large zones of calcification and of microcalcifications may involve cell-derived extracellular vesicles (EVs) that serve as nucleating foci for mineralization[18–20]. Emerging evidence suggests that vascular calcification involves calcifying EVs released from vascular smooth muscle cells (SMCs) and macrophages[18–20], implying that atherosclerotic plaques contain continuous sources of precursors of microcalcification. Yet, the process by which EVs contribute to vascular calcification remains unclear due to the inability to visualize and monitor early calcification events *in vivo*. Microcalcifications that create inhomogeneities in the fibrous cap cause a local accumulation of plaque-destabilizing stress[5], and therefore, understanding the contribution of this stress to plaque rupture requires a detailed study of the relationship between extracellular matrix components and microcalcification formation by EVs. *In silico* modeling indicates that calcification size, morphology, spacing, and collagen content combined contribute to plaque instability[5]. The present study aimed to understand the interaction of these factors by focusing on the mechanisms underlying the formation of the pathologic calcification, from microcalcifications to large calcifications. Advanced high-resolution imaging and material analysis techniques allowed for the characterization of human and mouse atherosclerotic plaques and an *in vitro* three-dimensional (3-D) type I

collagen hydrogel designed to mimic structural features of an atherosclerotic fibrous cap, served to permit direct observation of the processes of EV calcification nucleation and maturation. The results provide physicochemical mechanistic insight into the formation of plaque microcalcifications and the role of collagen in mediating this process.

Inverse correlation between collagen and calcification

High-resolution microcomputed tomography (μCT) revealed two different calcification morphologies within intact human coronary atherosclerotic plaques: microcalcifications (Fig. 1a, arrows) and large calcifications (Fig. 1b, dashed arrow). Microcalcifications can localize to the fibrous caps (Fig. 1a, yellow arrow). Deeper within the plaques microcalcifications appear to localize preferentially at regions corresponding to the borders of the lipid pool[21] (Fig. 1a, white arrow) and surround the large calcifications (Fig. 1b). Study of human carotid plaques showed similar calcification features (Fig. 1c). A 3-D reconstruction of μCT sections showed inhomogeneity of calcification throughout the vessel wall with regions of small (Fig. 1d, yellow arrow) and large calcifications (Fig. 1d, dashed arrow).

Using co-staining of von Kossa, identifying calcification, and picrosirius red, visualizing collagen under polarized light, this study assessed the relationship between collagen fiber structural organization and calcification morphology in human carotid atherosclerotic plaques (Fig. 1e–f). Overlapped images reveal large calcifications (> 200 μm) bordered by mature, aligned collagen fibers, as indicated by yellow-orange birefringence (Fig. 1e, 1f). A magnified polarized image of the region depicted by the white box shows dense, mature collagen fibers adjacent to the large calcification (Fig. 1g, dashed arrow). While not apparent in the low magnification images (Fig. 1e, red box), magnified images reveal microcalcifications stained brown-black by von Kossa (Fig. 1h, arrow). Microcalcifications localized to regions lacking collagen (Fig. 1i, arrow). Custom image analysis software color-coded thick collagen fibers red, thin collagen fibers green, and microcalcifications blue, allowing for the visualization of microcalcifications directly adjacent to collagen fibers (Fig. 1j, arrow).

Two-photon microscopy provided whole mount imaging of human carotid arteries. Optical sections of second harmonic generation signal from collagen fibers and near-infrared fluorescent calcium tracer signal were acquired from the luminal surface into the plaque, allowing observation of microcalcifications beneath the fibrous cap (Fig. 2a, yellow arrow) and a larger calcification deeper within the plaque (Fig. 2a, white arrow). A 3-D reconstruction viewed orthogonally to adjacent optical sections reveals microcalcifications within the fibrous cap as close as 20 μm from the lumen (Fig. 2b).

Confocal microscopy provided high-resolution, high-magnification imaging of plaque collagen and calcification within histologically sectioned carotid arteries (Fig. 2c). A custom green fluorescent agent[22] visualized collagen fibers and the near-infrared agent demonstrated calcification. Confocal images revealed abundant microcalcifications throughout the fibrous cap. The microcalcifications within the fibrous cap appeared to aggregate in gaps between collagen fibers and appeared as discrete spheres less than 1 μm in

diameter (Fig. 2c, arrows). Pearson correlation analysis revealed an inverse relationship between microcalcification area and collagen content within the analyzed regions of 200 μm^2 within the fibrous cap (Fig. 2d, n=9 patients, 24 regions per plaque, r=−0.29, p=0.01). Microcalcifications previously predicted to produce significant fibrous cap stress (~20 μm^2)[5,6] mainly localized in regions of low collagen content. The mean local collagen abundance of these microcalcifications was 16.5±14.8%. Microcalcifications surrounded regions of large calcifications (Fig. 2e).

EV aggregation correlates with mineralization

Density-dependent color scanning electron microscopy[17] (DDC-SEM, Fig. 3a) revealed structural heterogeneity within large calcific regions (orange hue indicates regions corresponding to calcium phosphate mineral) of a histological section of a carotid artery plaque. A magnified DDC-SEM image revealed small calcium phosphate-rich microcalcification spheres (<1 μm in diameter) appearing to aggregate to form the larger calcific region (Fig. 3b, arrow).

To test the hypothesis that the nucleation and growth of calcification depends on calcification and aggregation of cell-derived EVs, we developed a 3-D *in vitro* preparation to visualize these processes. Conditioned media containing EVs were collected over the course of 24 h from SMCs cultured in calcifying media and added to collagen hydrogels. After 72 h incubation with the collagen hydrogels, DDC-SEM revealed aggregation of EVs between collagen fibers (Fig. 3c), forming dense calcifying structures resembling those observed within calcified human plaques (Fig. 3b). Confocal reflection microscopy in gaps between collagen fibers identified EV aggregates (Fig. 3d, yellow arrow), which contained regions of calcification as detected by calcium tracer (Fig. 3d, insert). Supplemental Fig. 1 illustrates confirmation of the cellular origin of EV aggregates. Calcifying EV aggregates did not form in hydrogels incubated with EVs collected from SMCs cultured in control media.

Structured illumination super-resolution microscopy visualized aggregation and calcification of fluorescently labeled EVs (Fig. 3e–g). This technique allowed the visualization of objects the size of individual EVs (approximately 200 nm in diameter) localized within the collagen hydrogels (Fig. 3e, arrow). On these images, EVs appear to aggregate to produce spherical calcifying structures as indicated by a near-infrared fluorescent calcium tracer (Fig. 3f, g).

An image analysis algorithm assessed the volume of the aggregates identified by confocal reflection microscopy optical sections of the collagen hydrogels after 72 h incubation with the calcifying samples. Increasing the collagen concentration within the hydrogels reduced the average aggregate size by 90% compared to the samples without collagen (ANOVA, p<0.001).

We further explored the relationship between EV aggregation and mineral growth using nanoparticle-tracking analysis (NTA). After 1 day of incubation, EVs exhibited a size distribution profile corresponding to that previously described for calcifying EVs[23] (Fig. 3i, black line), and showed a shift to larger sizes over time, indicating EV aggregation (Fig. 3i, red line). Considerable aggregation occurred at the 5 and 7-day incubation times (Fig. 3j).

The shift in diameters measured by NTA corresponds to a concomitant increase in calcific mineral in the EVs quantified using a fluorescent-based detection[23] (Fig. 3k). The mineral content rose in calcifying vs. control samples after 5 and 7 days of incubation ($p < 0.001$). EVs obtained from control samples did not aggregate during the 7-day incubation (Supplemental Fig. 2).

Spectroscopic analytical methods provided insight into the mineral produced by aggregating EVs *in vitro*. Energy-dispersive x-ray spectroscopy (EDS) revealed that both small and large dense aggregate structures (Fig. 4a) contained high concentrations of both calcium and phosphate (Fig. 4a, inserts). EDS measurements obtained from a calcified human plaque revealed a calcium-phosphate ratio of 1.79±0.28 from microcalcifications and a ratio of 1.87±0.11 from large calcifications (n=8 per group), suggesting the presence of amorphous calcium phosphate mineral[17]. Following a 3-day incubation period, the calcium-phosphate ratio was 1.37±0.13, which increased to 1.94±0.02 after 5 days and 1.84±0.11 after 7 days, closely matching the values observed in the tissue (Supplemental Fig. 3). Previous studies suggested the amorphous nature of calcium phosphate mineral deposited in vascular tissues[17]. Similarly, TEM images of the calcifying EVs reveal an amorphous internal structure (Fig. 4b, c) with lower crystallinity, as shown by selected-area electron diffraction (Fig. 4b, insert).

Fourier transform infrared (FTIR) spectroscopy correlated EV aggregation with mineral composition, and the resulting spectra were compared with those obtained from a calcified carotid artery (Fig. 4d–g). Collagenase digestion of the EV-seeded hydrogels visualized calcific mineral as white crystalline structures (Fig. 4d, yellow arrows). Within a human carotid plaque (Fig. 4e), von Kossa staining revealed both microcalcifications (Fig. 4f, blue arrow) and large calcifications (Fig. 4f, red arrow). The FTIR spectrum from a sample of EVs isolated directly from SMCs in calcifying culture was considered as the initial time point without incubation in collagen hydrogels (Fig. 4g, Day 0). The remaining EVs in culture media were subsequently either placed directly into chambers (Fig. 4g, no collagen, lightest blue) or added to hydrogels with collagen concentrations of 0.1 mg/ml (Fig. 4g, medium blue) or 1 mg/ml (Fig. 4g, dark blue). The FTIR spectra after 1 or 5 day incubations were compared to the spectra from the human plaque microcalcification (Fig. 4g, Calcified Tissue, blue) and large calcification (Fig. 4g, Calcified Tissue, red).

A decrease in a FTIR absorbance peak at 1080 cm^{-1} and the appearance of absorbance peaks at 1020 cm^{-1} and 600 cm^{-1} signified calcific mineral maturation over the course of the 5-day incubation period in the EVs not added to collagen (Fig. 4g, lightest blue spectra). An absorbance peak at 875 cm^{-1} also increased in magnitude over the incubation period. These spectra changes agree with spectra for maturation of synthetic amorphous calcium phosphate[24,25]. Increasing collagen concentration in the hydrogels slowed calcification maturation over the course of 5 days. The FTIR spectrum from large calcification within human tissue revealed strong absorbance peaks at 1020 cm^{-1}, 875 cm^{-1}, and 600 cm^{-1} (Fig. 4g, Calcified Tissue, red), resembling the maturing mineral spectrum of EVs after 5 days with no collagen (Fig. 4g, Day 5, lightest blue). The FTIR spectrum from microcalcification within human plaque showed weaker peaks at 1080 cm^{-1} and 1020 cm^{-1} (Fig. 4g, Calcified Tissue, blue), resembling the immature spectra of EVs within the collagen hydrogels. The

observed correlation between mineral spectra maturity, aggregation time (*in vitro*), and calcification morphology (*in vivo*) indicates that microcalcifications serve as precursors to larger calcifications within the atherosclerotic plaque.

Collagen directs EV aggregation and calcification growth

These observations indicate that collagen acts as a scaffold, directing the aggregation and calcification of EVs. The establishment of a layered hydrogel structure to mimic the heterogeneity in collagen density observed *in vivo* helped demonstrate the effect of collagen on calcification morphology and growth (Supplemental Fig. 4). A high-density collagen hydrogel (2.5 mg/ml) overlapped with a low-density collagen hydrogel (0.1 mg/ml) created a continuous border (Fig. 5a). The addition of green fluorescently labeled EVs in calcifying media to the layered hydrogels, followed by blue-labeled EVs added 24 h later, helped monitor EV aggregation over time. Aggregates of green-labeled EVs and a few blue-labeled EVs localized throughout the low-density hydrogel and at the borders, but not within the high-density hydrogel at the 3-day mark (Fig. 5b, arrows). At day 7, aggregates containing calcified EVs labeled with both fluorophores aligned along the border of two collagen systems (Fig. 5c, arrows). These data paralleled the microcalcification alignment observed in human plaques using μCT.

Previous studies indicate that calcifying EVs trapped in an endogenous collagen matrix lead to mineral deposition in bone cell cultures[26,27]. Picrosirius red absorbance[28] demonstrated an increase in collagen accumulation in 21-day cultures of SMCs in calcifying media versus SMCs cultured in control media (Fig. 5d, $p<0.05$). After 14 days in calcifying media, a 3-D reconstruction of a confocal z-stack revealed the green fluorescently stained collagen fibers (Fig. 5e). Similar to the structures detected in human plaques, small microcalcifications entrapped by the collagen matrix appeared to merge, forming larger calcifications. After 21 days in calcifying media, both collagen fiber content and calcification area increased (Fig. 5f), revealing collagen entrapment of underlying calcification (Fig. 5g). A representative optical section taken by confocal microscopy shows the absence of calcification and collagen in control media cultures (Fig. 5h). A similar section obtained from SMCs in calcifying media illustrates small, spherical regions of calcification surrounding the SMCs, and orthogonal views of the confocal stack demonstrate the entrapment of the calcifications within collagen fibers (Fig. 5i). A magnified image of the calcified structures demonstrates aggregation of smaller substructures that lead to the mineral growth (Fig. 5j).

Apolipoprotein E–deficient ($Apoe^{-/-}$) mice on an atherogenic diet, develop calcification[29], and served to assess the role of collagen in mediating calcification growth *in vivo.* Longitudinal studies using intravital imaging of an intravenously injected near-infrared calcium tracer monitored progression of calcification growth in mouse carotid arteries. Quantification of the fluorescent signal shows a significant increase in calcification area from 20 to 30 weeks (Fig. 6b, n=6, $p=0.04$). Chronic kidney disease (CKD) accelerates the progression of calcification[30]. Fluorescence reflection imaging[29,31] helped image total aortic calcification in $Apoe^{-/-}$ mice and $Apoe^{-/-}$ mice with CKD induced by 5/6 nephrectomy. Accordingly, CKD-$Apoe^{-/-}$ mice exhibited a significant 6.1-fold increase in mean

calcification area when compared to *Apoe*$^{-/-}$ mice (Supplemental Fig. 5, n=6 per group, p<0.001).

A method commonly employed to detect the kinetics of bone remodeling[32] served to probe the conversion from microcalcifications to larger calcifications (Supplemental Fig. 6). The study used two different fluorescent calcium tracers injected intravenously into *Apoe*$^{-/-}$ mice: a calcein injection following 20 weeks of atherogenic diet and alizarin red S injection 3 weeks later. Imaging the green (calcein) and red (alizarin red S) fluorescence by confocal microscopy provided snapshots of the state of the aortic calcification at 20 and 23 weeks. Observations within the histological sections revealed green microcalcifications at 20 weeks (Fig. 6c, arrow) fully embedded within the alizarin red stained larger calcification that was formed by 23 weeks (Fig. 6c, dashed arrow). These data show that the microcalcifications present at the start of calcification become the core of the larger calcifications that develop over time.

The assessment of *Apoe*$^{-/-}$ mice and *Apoe*$^{-/-}$ mice deficient in matrix metalloproteinase 13 (MMP-13), a major collagen-degrading enzyme, allowed for the study of the role of collagen in mediating calcification growth *in vivo*[33]. Both groups consumed an atherogenic diet for 24 weeks, and were sacrificed and analyzed for collagen and calcification by histology. Consistent with previous studies[33], these mice exhibited increased plaque collagen content (Fig. 6d). Large calcifications solely formed in spaces between collagen fibers in *Apoe*$^{-/-}$ mice (Fig. 6d, arrows). Quantification of the inter-collagen spacing in each group shows significantly larger gaps in *Apoe*$^{-/-}$ mice compared to compound mutant *Apoe*$^{-/-}$/*Mmp13*$^{-/-}$ mice (Fig. 6e, n=8, p=0.03). The larger gaps between collagen fibers correlated to significantly larger calcification detected in the plaques of *Apoe*$^{-/-}$ mice than in the plaques of *Apoe*$^{-/-}$/*Mmp13*$^{-/-}$ mice (Fig. 6f, p=0.01). A histochemical stain for tissue non-specific alkaline phosphatase activity, an established marker of osteogenic activity, revealed no significant difference in the calcification potential of atherosclerotic plaques from *Apoe*$^{-/-}$ and *Apoe*$^{-/-}$/*Mmp13*$^{-/-}$ mice (Supplemental Fig. 7a, b, p=0.11). Dissolution of mineral within the plaques using hydrochloric acid also showed no differences in overall calcium content between *Apoe*$^{-/-}$ and *Apoe*$^{-/-}$/*Mmp13*$^{-/-}$ mice (Supplemental Fig. 7c, p = 0.91). These data indicate that, although similar calcification potentials exist between the two groups, the increased collagen in *Apoe*$^{-/-}$/*Mmp13*$^{-/-}$ mice significantly inhibits calcification growth.

Local collagen determines calcification morphology

Similar to previous studies, multimodal imaging of human atheroma reveal both large calcifications and spotty microcalcifications (Fig. 1, 2, 4), including potentially destabilizing microcalcifications within the fibrous cap (Fig. 1a, 2b, 2c). Clinical data and computational studies suggest that features of atherosclerotic plaque stability depend on calcification size and morphology and the fibrous cap collagen content[5]. The present study shows that microcalcification and collagen degradation, two factors that contribute to plaque rupture, interrelate. We documented an inverse relationship between collagen and the size of microcalcifications in human atherosclerotic plaques and 3-D hydrogel preparations. These

observations suggest that thinning of the fibrous cap accompanies microcalcification formation.

Microcalcification nucleation and growth occurs in four stages (Fig. 6g, insert). Localized collagen degradation within the plaque allows individual EVs to accumulate (Accumulation, Stage 1), followed by EV aggregation (Aggregation, Stage 2). Similar to processes previously described for fusion of liposomes[34,35], nucleation of calcium phosphate leads to fusion of the EV membranes (Fusion, Stage 3). Microcalcifications form due to the maturation of this mineral (Mineralization, Stage 4). Local collagen degradation within the cap thereby allows localized EV aggregation resulting in microcalcification formation (Fig. 6g). Matrix metalloproteinases, including macrophage-derived MMP-13, contribute to the paucity of fibrillar collagen[36] and even promote calcification[37]. Indeed, data from the present study show decreased size of calcified regions in the atherosclerotic plaques of $Apoe^{-/-}/Mmp13^{-/-}$ mice.

When unencumbered by collagen, microcalcifications serve as building blocks for larger calcifications. In human tissue, microcalcifications compose large calcifications, and experiments using injections of two calcium tracers in $Apoe^{-/-}$ mice show that microcalcifications present at 20 weeks of atherogenic diet coalesce into larger regions of calcification 3 weeks later. Therefore, microcalcifications and large calcifications exist as part of a continuum. The most important consideration is the contribution of individual calcifications to the mechanical stability of plaques. Computational analyses indicate that microcalcifications of approximately 5 μm in diameter that localize within a collagen-poor fibrous cap, increase mechanical stress within the hyperelastic tissue surrounding microcalcification inclusions and favor rupture. While the theoretical analysis of explosive growth of small voids occurs when the local tissue stress exceeds the local Young's modulus of the tissue, this growth is unlikely to occur if the microcalcifications are smaller than 5 μm. Notably, microcalcifications formed in the collagen hydrogels used in this study often approached the size threshold previously calculated to lead to plaque destabilization[5,6].

Previous studies also demonstrated that elongated ellipsoidal microcalcifications result in significantly higher stress at the poles of the long axis than spherical microcalcifications[38]. The present study's results indicate that these structures form by aggregation of adjacent microcalcifications between collagen fibers, and that alignment of collagen within the fibrous cap facilitates association of the microcalcifications to assume this elongated morphology. The current study did not assess the direct physical interaction between collagen and calcification, and the *in vitro* structures did not include factors that may mediate this interaction such as proteoglycans. Future work on the mechanisms of calcification incorporation into the tissue may enhance the understanding of the physical phenomena that favor plaque rupture.

Future studies into the role of plaque lipids and matrix changes on cellular behavior will be important in identifying points of therapeutic intervention. Collagen accumulation and large calcification in fibrous caps increases the tensile strength of the plaques[39] but also increases the total plaque stiffness. Recent findings suggest that oxidized LDL cholesterol can induce SMCs to adopt a calcific phenotype[40] and that cells undergo osteogenic differentiation

following matrix stiffening[41]. Elucidating these mechanisms will provide insight into the cellular source of calcifying extracellular vesicles within the plaque.

Outlook

The approaches used here can enable future studies to control mineral nucleation and growth in a search for therapeutic strategies to limit vascular calcification. Most clinical studies of calcification use intravascular ultrasound, magnetic resonance, or optical coherence tomography imaging. These techniques have a lower resolution threshold of 30–50 μm, limiting their ability to identify high-risk microcalcifications. Advanced imaging techniques that can identify inflammation and calcification within potentially vulnerable plaques in patients now exist[42]. New insight into the mechanisms associated with calcification formation and growth may inform clinical decisions into appropriate interventions in these patients. Gaining this insight will continue to require detailed analyses on the impact of calcific remodeling on tissue material properties and plaque instability.

Local stress maxima directly adjacent to microcalcifications within the fibrous cap induce plaque rupture[5,38]. Future studies may build on the current work by using nano-analytical techniques such as atomic force microscopy to probe the local stresses in the extracellular matrix surrounding microcalcifications. Many previous computational studies have modeled the fibrous cap as a homogenous hyperelastic material[5,6]. These analyses have provided important insight into our initial understanding of the role of microcalcifications in plaque rupture. The current study, however, illustrates the inhomogeneity of the extracellular matrix surrounding microcalcifications and the importance of local collagen remodeling in microcalcification formation. Therefore, new analyses into the stresses associated with this localized remodeling may help to refine the computational models and provide insight into means to therapeutically alter the stresses by targeting local extracellular components, thereby preventing plaque failure.

Methods

MicroCT of coronary arteries

Human coronary artery specimens were scanned using a high-resolution microcomputed tomography (μCT) system (SkyScan 1172). μCT system energy settings were chosen to increase the contrast between soft tissue, atheroma's lipid content, and the mineralized tissue. Each scan produced approximately 8,000 2-dimensional slices of 2,000 × 2,000 in-plane matrix, with 2.1-μm isotropic voxel resolution and 8-bit gray levels. The 2-dimensional slices were then used to create a 3-dimensional view of the artery specimens.

Histological analyses

Atherosclerotic carotid arteries (n=30) were obtained from patients undergoing endarterectomy surgery or from autopsy at Brigham and Women's Hospital according to Institutional Review Board protocols. Samples were embedded in OCT compound and stored at −80 °C until use. Tissue was cut into 7 μm-thin sections for further analyses. Either a near-infrared bisphosphonate-based calcium tracer (OsteoSense 680, Perkin Elmer) or von Kossa phosphate staining was used to identify calcification within the sections. The calcium

tracer was diluted 1:100 from the original stock and was applied to the sections overnight at 4 °C. Collagen in the plaques was identified by staining sections with either a fluorescently conjugated collagen probe or utilizing picrosirius red staining and imaging with polarized light microscopy. When visualized under polarized light, picrosirius red exhibits birefringence that distinguishes mature thick collagen bundles (yellow-orange hue) from immature or disrupted thin collagen fibers (green hue)[43]. Prior to bright field, polarized light, or confocal imaging, sections were washed in PBS and embedded in mounting medium containing DAPI (Vector Laboratories).

Two photon and confocal microscopy

Second harmonic generation using two photon microscopy (Zeiss LSM 780 NLO) was employed to image collagen fibers within non-sectioned human carotid arteries. Following resection, the arteries were fixed for 48 h in 4% paraformaldehyde at 4 °C. The intact arteries were then washed in PBS and cut longitudinally into two portions to reveal the lumen face of the vessels. The arteries were then incubated with a near-infrared bisphosphonate-based calcium tracer (OsteoSense 680, Perkin Elmer) diluted 1:100 from the original stock for 48 h at 4 °C. Following this incubation, the arterial segments were washed thoroughly with PBS and the media sides of the arteries were affixed to 6 cm diameter cell culture dishes using super glue such that the lumen sides of the arteries were facing up. PBS was added to completely submerge the segments. Optical section images were collected from the lumen side of the artery up to 300 μm into the plaque using a step size of 1 μm. This method allowed us to simultaneously image calcification and collagen orientation in plaques without disruptive effects of histological sectioning. Collagen was identified by analysis of second harmonic generation signal, and calcification was delineated using continuous-wave confocal microscopic imaging of the near-infrared calcium tracer. Second harmonic signal was generated by tuning the Mai Tai Ti:sapphire laser to 850 nm and collecting the resultant tissue emission at 425 nm. These images were overlaid with corresponding optical sections of fluorescent detection of the near-infrared bisphosphonate-based calcium tracer using continuous wave confocal imaging.

Continuous wave confocal microscopy (Nikon A1) was used to image histological sections of human carotid arteries and collagen hydrogels. Fluorescent images were obtained at specific excitation and emission wavelengths using the imaging software. Confocal reflection images were utilized to image collagen fibers within the hydrogels and were collected by setting the excitation wavelength to 514 nm and collecting the emitted light using a 520/10 nm band pass filter.

Quantitative image analyses

To overlay microcalcifications identified by bright field histological imaging onto polarized images of collagen fibers, we utilized a modified image analysis algorithm based upon our published hue saturation value program available at cics.partners.org[44]. Our custom software identified microcalcifications that exhibit a brown hue following von Kossa staining. These microcalcifications were assigned a blue pseudo-color and overlaid onto the corresponding polarized light of picrosirius red stained collagen fibers wherein mature collagen fibers were pseudo-colored red and immature collagen fibers were pseudo-colored green. A similar

analysis was utilized to identify collagen fibers in apoE$^{-/-}$/MMP13$^{-/-}$ mice. Inversion of the images allowed identification and quantification of intercollagen area.

A custom image analysis algorithm (MatLab) helped quantify the amount of collagen surrounding microcalcifications observed within the atherosclerotic plaques of carotid arteries resected from 9 different human patients. MatLab code can be provided by the corresponding author. Microcalcifications were identified as regions with more than 4 connected pixels positive for fluorescence from the bisphosphonate calcium tracer. A control area of 200 μm^2 was analyzed for collagen content surrounding each microcalcification. The normalized collagen amount was calculated by dividing the pixels of collagen fluorescence by the total pixels within the region. A similar custom algorithm was used to quantify the volume of EV aggregates observed within collagen hydrogels; for these analyses, however, z-stack optical sections were used to identify the 3-dimensional structure of the aggregates. The average aggregate volume for each gel was determined, and 4 independent hydrogels of each collagen concentration considered were analyzed.

Density-dependent color SEM

For density-dependent color scanning electron microscopy (DDC-SEM) imaging, histologically sectioned samples, intact collagen hydrogels, or collagenase isolated hydrogel components on a glass slide were secured to an aluminum sample holder with carbon tape, and silver paint was applied to the area immediately surrounding each sample, which was then coated with 5nm carbon (Quorum Technologies Turbo-Pumped Thermal Evaporators model K975X) and 5nm chromium in a sputter coater (Quorum Technologies Sputter Coater model K575X). Following the coating procedure, samples were imaged by an SEM (Gemini 1525 FEGSEM), operated at 10 kV. The instrument was equipped with both an inlens detector that recorded secondary electrons, and a backscatter electron detector. The DDC-SEM images were obtained by imaging a region in inlens mode and subsequently imaging the same region in backscatter mode. Using ImageJ software, both images were stacked and the inlens image was assigned to the green channel whereas the backscatter image was assigned to the red channel.

Elemental and mineral structure analyses

Energy-dispersive x-ray spectroscopy was used to characterize mineral content in both histological sections of calcified human carotid arteries and calcific structures from collagen hydrogels. The calcium to phosphate ratio determined by EDS commonly identifies the type of mineral present in calcified materials. For the collagen hydrogel analyses, 1 mg/ml collagenase in PBS was used to digest the collagen following the experimental incubation period, and the calcified EV aggregates from the hydrogels were collected by ultracentrifugation at 100,000 × g for 40 min. Following the EDS analyses, the structures were sectioned using a focused gallium ion beam, and selected-area electron diffraction and transmission electron microscopy (TEM) were utilized to assess the crystallinity of the structures.

Fourier transform infrared spectroscopy (Bruker, FTIR) was also utilized to perform elemental analyses of both histological sections of calcified human carotid arteries and

calcific structures from collagen hydrogels. The FTIR system contains a motorized stage and polarized optical microscope to identify regions of interest. Attenuated total reflectance mode (single bounce Ge crystal) was used to collect spectral data in a range from 4,000 to 600 cm^{-1}.

Cell culture and EV collection

Human coronary artery smooth muscle cells (SMCs; PromoCell) were grown to confluence and cultured in control media consisting of DMEM with 10% fetal bovine serum and 1% penicillin/streptomycin or a calcifying media consisting of control media supplemented with 10 nM dexamethasone, 100 μM L-ascorbic acid, and 10 mM β-glycerolphosphate. The media were replaced every two days. The SMCs were cultured for at least 14 days, a time point sufficient to induce calcific differentiation of the cells in the calcifying media[45]. After the prescribed culture period, the culture media were replaced with media containing the same components but lower fetal bovine serum (0.1%) to reduce the noise caused by the presence of vesicles within the serum compared to the vesicles of interest released by SMCs. After 24 h, the low serum media was collected after centrifugation at 1,000 × g for 5 min to remove potential cellular contaminants and large vesicles such as apoptotic bodies. The resulting supernatant was then stored at −80 °C prior to further processing. EVs were isolated from the supernatant by ultracentrifugation at 100,000×g for 40 min and resuspended in fresh control or calcifying media. A portion of the conditioned media for each sample was reserved for nanoparticle tracking analysis to ensure the absence of larger vesicles such as apoptotic bodies.

Collagen hydrogel experiments

Collagen hydrogels were made by slowly raising the pH of high concentration rat tail collagen stored in a solution of acetic acid (BD Biosciences) to 7–8. In this pH range, the collagen forms a hydrogel network. The neutralized collagen solution was then added to chambered coverglass wells (LAB-TEK, #1.5 borosilicate). EVs in SMC conditioned media with 0.1% FBS were then added to the collagen network and incubated at 37 °C for the indicated time period. One day prior to imaging, a near-infrared based bisphosphonate calcium tracer (OsteoSense 680, Perkin Elmer) was added to the hydrogels and incubated overnight at 37 °C. The resulting aggregation and calcification processes were imaged by confocal fluorescence and reflection microscopy.

To create layered collagen hydrogels, a 15 μl volume of 2.5 mg/ml collagen solution was pipetted onto the surface of a chambered well glass. After 1 h incubation at 37 °C, a 15 μl volume of 0.1 mg/ml collagen solution was placed directly adjacent to the first cast hydrogel such that the two drops formed a continuous border. CellTracker (Invitrogen) dyes were used to fluorescently label EVs prior to addition to the hydrogels. After crossing the cellular plasma membrane, CellTracker fluorescent dyes are converted by intracellular enzymes to a membrane impermeant form that is well retained in the cellular cytoplasm. We added CellTracker to the conditioned media containing EVs from SMCs at 2.5 μM for 30 min. Chromatography columns (GE Healthcare PD-10 columns) helped remove the dye solution per manufacturer’s protocol. After the EV portion was collected from the column, the EVs

were pelleted by ultracentrifugation at 100,000 × g for 40 min and re-suspended in dye free media prior to being added to collagen hydrogels.

Nanoparticle tracking analyses (NTA)

NTA by NanoSight LM10 (Malvern Instruments Ltd, Malvern, UK) assessed vesicle size and concentration within the media samples[46]. Calcific SMC-derived EVs collected from conditioned media by ultracentrifugation at 100,000 × g were resuspended in 1 ml calcifying media and divided into five 200 μl portions. One portion was collected for initial time point analyses. Aggregation was detected by NTA in the remaining portions incubated at 37 °C for 1, 3, 5, or 7 days. NTA determines nanoparticle number and size distributions from the Brownian motions of objects illuminated by laser light[47]. The samples were diluted 1:7 in PBS prior to injection into the NanoSight chamber. Samples were continuously injected via a syringe pump (Malvern), and five NTA videos were collected for 1 min each. The camera gain was set at a constant value of 9, and the threshold value for vesicle detection was set to 2. The resultant size and concentration output data from each video were averaged to generate the final distribution for each sample.

EV mineralization assay

Utilization of a fluorescence-based dye (OsteoImage, Lonza) allowed quantification of mineral within EVs. Briefly, isolated EVs were resuspended in 200 μl diluted OsteoImage dye (according to manufacturer protocol) for 30 min at room temperature. The dye was then removed via ultracentrifugation and the vesicles were washed twice in OsteoImage wash buffer using 100,000 × g ultracentrifugation for 40 min. After the final wash, the pellet was resuspended in 100 μl OsteoImage wash buffer and fluorescence intensity was measured using a plate reader.

Sircol quantitative collagen assay

Collagen content of SMCs in culture was determined in the extracellular matrix using Sircol Soluble Collagen Assay (Biocolor, Northern Ireland, UK) based on picrosirius red dye. Briefly, after a washing step, cells were incubated with 0.5 M acetic acid and 0.1 mg/ml pepsin overnight. After neutralization, collagen was concentrated overnight. The next day, Sircol reagent was added to bind collagen. After two washing steps the Sircol dye was released from the collagen-dye complex by alkali reagent and absorption at 555 nm was measured.

Structure Illumination Microscopy

Structure illumination microscopy (Zeiss ELYRA Super-Resolution) allowed high resolution imaging of fluorescently labeled EVs within collagen hydrogels. Prior to imaging, a near-infrared based bisphosphonate calcium tracer (OsteoSense 680, Perkin Elmer) was added to the hydrogels and incubated overnight at 37 °C. To minimize refractive index mismatch, hydrogels were serially immersed in solutions with increasing concentration of 2,2′-thiodiethanol (TDE) (Sigma Aldrich) (10%, 25%, 50%, 97% three times, all at pH 7.5 +/−1) as previously described[48] and mounted in 95% TDE medium with 2.4% anti-fade 1,4-Diazabicyclo[2,2,2]octane solution, or DABCO (Sigma Aldrich). Samples were covered

with high precision cover glass (No. 1.5H, 170±5 μm) (Biosciencetools). SIM imaging improves the resolution of traditional fluorescence and confocal microscopy from approximately 300 nm down to 100 nm[49].

Calcification in mouse atherosclerotic plaques

The intravital imaging, fluorescence reflection imaging, and *Apoe*$^{-/-}$/*Mmp13*$^{-/-}$ mouse data reported in this study were obtained from unused tissues or analyses from previous studies as cited, and all experiments were performed in accordance with procedures approved by Institutional Animal Care and Use Committees. For intravital imaging, 10 week old *Apoe*$^{-/-}$ mice consumed an atherogenic diet for 10 weeks. Mice received intravenous injection of a bisphosphonate-derivatized near-infrared imaging agent (OsteoSense) according to manufacturer's protocol 24 h before imaging. A small incision revealed the mouse carotid artery, and an intravital laser scanning microscope detected fluorescence following excitation at 748 nm. Following suturing of the incision, the mice resumed the atherogenic diet for 10 additional weeks. Repeating the intravital imaging procedure on the same carotid artery imaged 10 weeks earlier allowed monitoring of the calcification progression.

A two-step 5/6 nephrectomy procedure created CKD-*Apoe*$^{-/-}$ mice. These mice also received an atherogenic diet at 10 weeks of age for 10 weeks. The mice were euthanized 24 h following intravenous injection of the near-infrared bisphosphonate-derivatized agent, and excision of heart and major arteries allowed fluorescence reflectance imaging to map the cardiovascular osteogenic activity. Control *Apoe*$^{-/-}$ received a sham surgery but retained normal kidney function. Calcein green and alizarin red S allowed tracing of calcification growth in atherosclerotic plaques apoE$^{-/-}$ mice over time. Beginning at 10 weeks of age, the mice received an atherogenic diet for 20 weeks. An intravenous injection of calcein green labeled the existing calcification *in situ*. The mice continued to receive the atherogenic diet for 3 additional weeks followed by an intravenous injection of alizarin red S to label the calcification at this time point. Mice were euthanized three days later. Confocal microscopy of histological sections imaged the fluorescence signal liberated from these two dyes.

Age-matched *Apoe*$^{-/-}$ controls and 8-to-10 week old *Apoe*$^{-/-}$/*Mmp13*$^{-/-}$ mice received an atherogenic diet for 24 weeks. Following euthanization, histopathologic sectioning of the aortic root allowed for analyses of collagen, TNAP, and calcification within atherosclerotic plaques. TNAP was identified using a colorimetric substrate kit (VECTOR Laboratories), and calcium was extracted from four histological sections per mouse per group through an overnight incubation at 37 °C with 0.6 M hydrochloric acid. Calcium in the extract was measured using colorimetric assay kit (BioVision).

Statistical analyses

Quantitative data are given as mean ± standard deviation, and n indicates the number of independent experiments. Neither the experiments nor outcomes were blinded during the study. Statistical packages within GraphPad Prism determined data normality and estimated the variance between groups of data. Statistical differences were determined using a one-way ANOVA with Bonferroni's post hoc test, and single group comparisons using a Student's t test with significance considered as $p<0.05$. Unless otherwise noted, statistical

differences from *in vitro* experiments were determined using three different human SMC donors to ensure that observations were not skewed by a single outlier SMC culture. Correlative analyses were performed using a Pearson correlation method. A paired t test determined significance in the time course intravital imaging experiments. A Mann-Whitney U test assessed significant differences in the non-normally distributed results obtained from the comparison of calcification areas in $Apoe^{-/-}$ and $Apoe^{-/-}/Mmp13^{-/-}$ mice.

Supplementary Material

Refer to Web version on PubMed Central for supplementary material.

Acknowledgments

This work was supported by a research grant from Kowa Company Ltd. to Dr. Masanori Aikawa. Dr. Elena Aikawa is supported by grants from the National Institutes of Health (R01HL114805; R01HL109506) and a Harvard Catalyst Advanced Microscopy Pilot Award. The Harvard Clinical and Translational Science Center (National Center for Research Resources and the National Center for Advancing Translational Sciences, National Institutes of Health Award UL1 TR001102) and financial contributions from Harvard University and its affiliated academic healthcare centers. The content is solely the responsibility of the authors and does not necessarily represent the official views of Harvard Catalyst, Harvard University and its affiliated academic healthcare centers, or the National Institutes of Health. Dr. Libby is supported by R01HL80472. The authors thank Tan Pham, Jung Choi, and Brett Pieper for technical assistance and Chelsea Swallom for editorial expertise. Tanya Holmes and Michelle Siciliano from the Brigham and Women's Hospital Anatomic Pathology Laboratory graciously provided human autopsy tissue. Dr. Galina Sukhova provided surgically resected carotid artery tissue from endarterectomy patients at Brigham and Women's Hospital. Dr. Sasha Singh contributed valuable insight into data interpretation and presentation. Two photon microscopy and structure illumination imaging were performed at the Harvard Center for Biological Imaging. Dr. Sergio Bertazzo was supported by the Junior Research Fellowship scheme from Imperial College London.

References

1. Mozaffarian D, et al. Heart disease and stroke statistics--2015 update: a report from the American Heart Association. Circulation. 2015; 131:e29–322. [PubMed: 25520374]
2. Murray CJ, Lopez AD. Measuring the global burden of disease. The New England journal of medicine. 2013; 369:448–457. [PubMed: 23902484]
3. Libby P. Collagenases and cracks in the plaque. The Journal of clinical investigation. 2013; 123:3201–3203. [PubMed: 23908120]
4. Libby P. Mechanisms of acute coronary syndromes and their implications for therapy. The New England journal of medicine. 2013; 368:2004–2013. [PubMed: 23697515]
5. Kelly-Arnold A, et al. Revised microcalcification hypothesis for fibrous cap rupture in human coronary arteries. Proceedings of the National Academy of Sciences of the United States of America. 2013; 110:10741–10746. [PubMed: 23733926]
6. Maldonado N, Kelly-Arnold A, Cardoso L, Weinbaum S. The explosive growth of small voids in vulnerable cap rupture; cavitation and interfacial debonding. Journal of biomechanics. 2013; 46:396–401. [PubMed: 23218838]
7. Maldonado N, et al. A mechanistic analysis of the role of microcalcifications in atherosclerotic plaque stability: potential implications for plaque rupture. Am J Physiol Heart Circ Physiol. 2012; 303:H619–628. [PubMed: 22777419]
8. Vliegenthart R, et al. Coronary calcification improves cardiovascular risk prediction in the elderly. Circulation. 2005; 112:572–577. [PubMed: 16009800]
9. Martin SS, et al. Dyslipidemia, coronary artery calcium, and incident atherosclerotic cardiovascular disease: implications for statin therapy from the multi-ethnic study of atherosclerosis. Circulation. 2014; 129:77–86. [PubMed: 24141324]

10. Vengrenyuk Y, et al. A hypothesis for vulnerable plaque rupture due to stress-induced debonding around cellular microcalcifications in thin fibrous caps. Proceedings of the National Academy of Sciences of the United States of America. 2006; 103:14678–14683. [PubMed: 17003118]
11. Criqui MH, et al. Calcium density of coronary artery plaque and risk of incident cardiovascular events. JAMA: the journal of the American Medical Association. 2014; 311:271–278. [PubMed: 24247483]
12. Lin TC, et al. Mechanical response of a calcified plaque model to fluid shear force. Annals of biomedical engineering. 2006; 34:1535–1541. [PubMed: 17006755]
13. Imoto K, et al. Longitudinal structural determinants of atherosclerotic plaque vulnerability: a computational analysis of stress distribution using vessel models and three-dimensional intravascular ultrasound imaging. Journal of the American College of Cardiology. 2005; 46:1507–1515. [PubMed: 16226176]
14. Wong KK, Thavornpattanapong P, Cheung SC, Sun Z, Tu J. Effect of calcification on the mechanical stability of plaque based on a three-dimensional carotid bifurcation model. BMC cardiovascular disorders. 2012; 12:7. [PubMed: 22336469]
15. Holzapfel GA, Mulvihill JJ, Cunnane EM, Walsh MT. Computational approaches for analyzing the mechanics of atherosclerotic plaques: a review. Journal of biomechanics. 2014; 47:859–869. [PubMed: 24491496]
16. Ehara S, et al. Spotty calcification typifies the culprit plaque in patients with acute myocardial infarction: an intravascular ultrasound study. Circulation. 2004; 110:3424–3429. [PubMed: 15557374]
17. Bertazzo S, et al. Nano-analytical electron microscopy reveals fundamental insights into human cardiovascular tissue calcification. Nature materials. 2013; 12:576–583. [PubMed: 23603848]
18. New SE, et al. Macrophage-derived matrix vesicles: an alternative novel mechanism for microcalcification in atherosclerotic plaques. Circ Res. 2013; 113:72–77. [PubMed: 23616621]
19. Kapustin AN, et al. Calcium regulates key components of vascular smooth muscle cell-derived matrix vesicles to enhance mineralization. Circulation research. 2011; 109:e1–12. [PubMed: 21566214]
20. Anderson HC. Matrix vesicles and calcification. Current rheumatology reports. 2003; 5:222–226. [PubMed: 12744815]
21. Maldonado N, Kelly-Arnold A, Laudier D, Weinbaum S, Cardoso L. Imaging and analysis of microcalcifications and lipid/necrotic core calcification in fibrous cap atheroma. The international journal of cardiovascular imaging. 2015; 31:1079–1087. [PubMed: 25837377]
22. Krahn KN, Bouten CV, van Tuijl S, van Zandvoort MA, Merkx M. Fluorescently labeled collagen binding proteins allow specific visualization of collagen in tissues and live cell culture. Analytical biochemistry. 2006; 350:177–185. [PubMed: 16476406]
23. Hutcheson JD, et al. Enrichment of calcifying extracellular vesicles using density-based ultracentrifugation protocol. Journal of extracellular vesicles. 2014; 3:25129. [PubMed: 25491249]
24. Pleshko N, Boskey A, Mendelsohn R. Novel infrared spectroscopic method for the determination of crystallinity of hydroxyapatite minerals. Biophysical journal. 1991; 60:786–793. [PubMed: 1660314]
25. Gadaleta SJ, Paschalis EP, Betts F, Mendelsohn R, Boskey AL. Fourier transform infrared spectroscopy of the solution-mediated conversion of amorphous calcium phosphate to hydroxyapatite: new correlations between X-ray diffraction and infrared data. Calcified tissue international. 1996; 58:9–16. [PubMed: 8825233]
26. Thouverey C, et al. Proteomic characterization of biogenesis and functions of matrix vesicles released from mineralizing human osteoblast-like cells. Journal of proteomics. 2011; 74:1123–1134. [PubMed: 21515422]
27. Xiao Z, et al. Analysis of the extracellular matrix vesicle proteome in mineralizing osteoblasts. Journal of cellular physiology. 2007; 210:325–335. [PubMed: 17096383]
28. Walsh BJ, Thornton SC, Penny R, Breit SN. Microplate reader-based quantitation of collagens. Analytical biochemistry. 1992; 203:187–190. [PubMed: 1384382]
29. Aikawa E, et al. Osteogenesis associates with inflammation in early-stage atherosclerosis evaluated by molecular imaging in vivo. Circulation. 2007; 116:2841–2850. [PubMed: 18040026]

30. Aikawa E, et al. Arterial and aortic valve calcification abolished by elastolytic cathepsin S deficiency in chronic renal disease. Circulation. 2009; 119:1785–1794. [PubMed: 19307473]
31. Aikawa E, et al. Multimodality molecular imaging identifies proteolytic and osteogenic activities in early aortic valve disease. Circulation. 2007; 115:377–386. [PubMed: 17224478]
32. Goettsch C, et al. NADPH oxidase 4 limits bone mass by promoting osteoclastogenesis. The Journal of clinical investigation. 2013; 123:4731–4738. [PubMed: 24216508]
33. Quillard T, Araujo HA, Franck G, Tesmenitsky Y, Libby P. Matrix metalloproteinase-13 predominates over matrix metalloproteinase-8 as the functional interstitial collagenase in mouse atheromata. Arteriosclerosis, thrombosis, and vascular biology. 2014; 34:1179–1186.
34. Fraley R, Wilschut J, Duzgunes N, Smith C, Papahadjopoulos D. Studies on the mechanism of membrane fusion: role of phosphate in promoting calcium ion induced fusion of phospholipid vesicles. Biochemistry. 1980; 19:6021–6029. [PubMed: 7470446]
35. Wilschut J, Duzgunes N, Fraley R, Papahadjopoulos D. Studies on the mechanism of membrane fusion: kinetics of calcium ion induced fusion of phosphatidylserine vesicles followed by a new assay for mixing of aqueous vesicle contents. Biochemistry. 1980; 19:6011–6021. [PubMed: 7470445]
36. Deguchi JO, et al. Matrix metalloproteinase-13/collagenase-3 deletion promotes collagen accumulation and organization in mouse atherosclerotic plaques. Circulation. 2005; 112:2708–2715. [PubMed: 16230484]
37. Nishimura R, et al. Osterix regulates calcification and degradation of chondrogenic matrices through matrix metalloproteinase 13 (MMP13) expression in association with transcription factor Runx2 during endochondral ossification. J Biol Chem. 2012; 287:33179–33190. [PubMed: 22869368]
38. Cardoso L, Kelly-Arnold A, Maldonado N, Laudier D, Weinbaum S. Effect of tissue properties, shape and orientation of microcalcifications on vulnerable cap stability using different hyperelastic constitutive models. Journal of biomechanics. 2014; 47:870–877. [PubMed: 24503048]
39. Ruiz JL, Hutcheson JD, Aikawa E. Cardiovascular calcification: current controversies and novel concepts. Cardiovascular pathology: the official journal of the Society for Cardiovascular Pathology. 2015
40. Goettsch C, et al. Nuclear factor of activated T cells mediates oxidised LDL-induced calcification of vascular smooth muscle cells. Diabetologia. 2011; 54:2690–2701. [PubMed: 21701818]
41. Yang C, Tibbitt MW, Basta L, Anseth KS. Mechanical memory and dosing influence stem cell fate. Nature materials. 2014; 13:645–652. [PubMed: 24633344]
42. Adamson PD, Vesey AT, Joshi NV, Newby DE, Dweck MR. Salt in the wound: (18)F-fluoride positron emission tomography for identification of vulnerable coronary plaques. Cardiovascular diagnosis and therapy. 2015; 5:150–155. [PubMed: 25984456]
43. Whittaker P, Kloner RA, Boughner DR, Pickering JG. Quantitative assessment of myocardial collagen with picrosirius red staining and circularly polarized light. Basic research in cardiology. 1994; 89:397–410. [PubMed: 7535519]
44. Yabusaki K, et al. A novel quantitative approach for eliminating sample-to-sample variation using a hue saturation value analysis program. PloS one. 2014; 9:e89627. [PubMed: 24595280]
45. Steitz SA, et al. Smooth muscle cell phenotypic transition associated with calcification: upregulation of Cbfa1 and downregulation of smooth muscle lineage markers. Circulation research. 2001; 89:1147–1154. [PubMed: 11739279]
46. Filipe V, Hawe A, Jiskoot W. Critical evaluation of Nanoparticle Tracking Analysis (NTA) by NanoSight for the measurement of nanoparticles and protein aggregates. Pharmaceutical research. 2010; 27:796–810. [PubMed: 20204471]
47. Wright M. Nanoparticle tracking analysis for the multiparameter characterization and counting of nanoparticle suspensions. Methods in molecular biology. 2012; 906:511–524. [PubMed: 22791460]
48. Staudt T, Lang MC, Medda R, Engelhardt J, Hell SW. 2,2′-thiodiethanol: a new water soluble mounting medium for high resolution optical microscopy. Microscopy research and technique. 2007; 70:1–9. [PubMed: 17131355]

49. Langhorst MF, Schaffer J, Goetze B. Structure brings clarity: structured illumination microscopy in cell biology. Biotechnology journal. 2009; 4:858–865. [PubMed: 19492328]

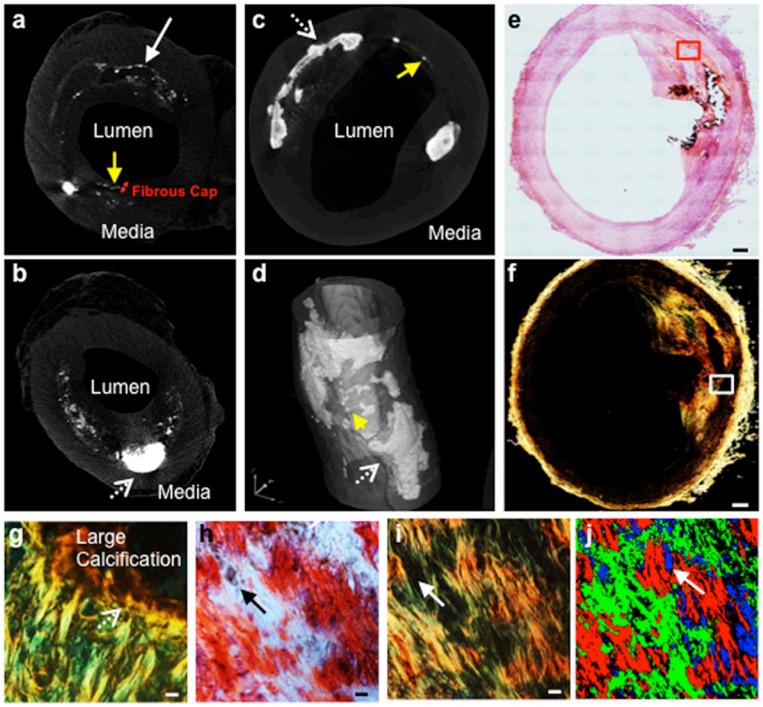

Fig. 1.

Identification of calcific morphologies within human atherosclerotic plaques. a) Apical view from a μCT scan of a coronary artery with microcalcifications throughout the plaque (white arrow) and in the fibrous cap (yellow arrow). b) Apical view from a μCT scan of a coronary artery with large calcification (dashed arrow). c) Apical view from a μCT scan of a carotid artery with large calcification (dashed arrow) and microcalcifications (yellow arrow). d) Three-dimensional reconstruction of μCT sections of a carotid artery with large (dashed arrow) and small (yellow arrow) calcifications. e) Composite bright field image of a histological section of a human carotid artery with an atherosclerotic plaque. Von Kossa staining was used to identify regions of calcification (arrow, scale = 500 μm). f) Composite polarized image of a histological section of a human carotid artery with an atherosclerotic plaque. Picrosirius red staining helped identify collagen fibers (scale = 500 μm). g) Magnified polarized image of large calcification region (dashed arrow, scale = 25 μm). h) Magnified bright field image revealing microcalcification (arrow, scale = 25 μm). i) Polarized image of microcalcification region (arrow, scale = 25 μm). j) Bright field and polarized image overlay with digital pseudo-color showing mature collagen (red), immature collagen (green), and microcalcifications (blue, arrow).

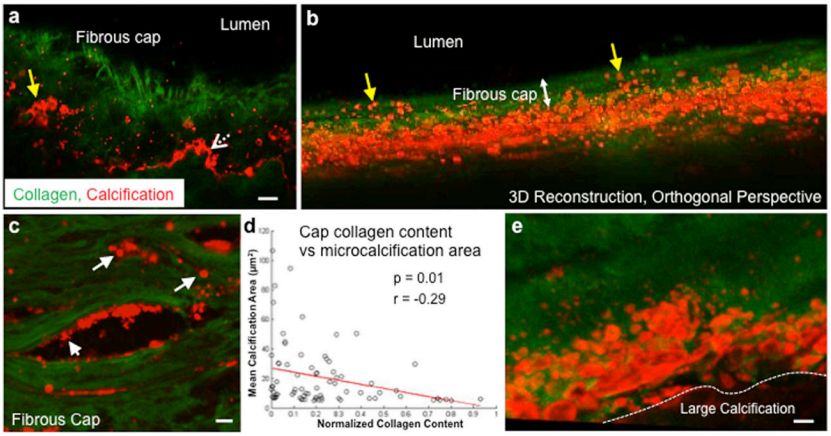

Fig. 2.

Collagen and calcification structure in human carotid artery atherosclerotic plaques. a) Two-photon microscopy second harmonic generation of collagen (green) overlayed with continuous wave confocal microscopy identification of a near-infrared calcium tracer (red) in a calcified human carotid atherosclerotic plaque. (scale = 20 μm) b) Orthogonal view of 3-dimensional reconstruction of two-photon and continuous wave confocal z-stacks demonstrating the fibrous cap (white arrow) with microcalcifications (yellow arrows). c) Confocal optical section of microcalcifications (arrows) within a human carotid artery fibrous cap stained with a near-infrared calcium tracer (red) and a custom collagen probe (green). (scale = 20 μm) d) Quantification of collagen content surrounding microcalcifications identified across 9 different human plaques. Correlation determined by Pearson method (red line, n=9, p=0.01). e) Confocal 3-dimensional reconstruction of optical sections of a large calcification within a human carotid artery plaque stained with a near-infrared calcium tracer (red) and a custom collagen probe (green). (scale = 20 μm)

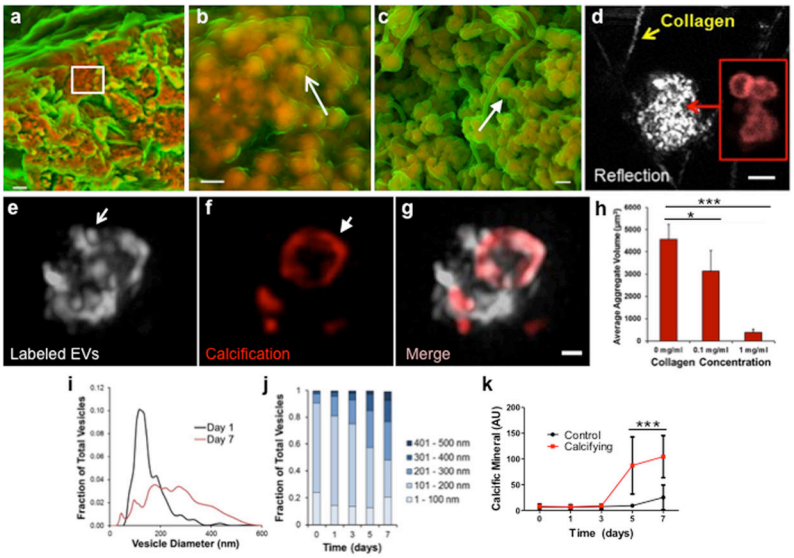

Fig. 3.

EV aggregation and calcification in calcified tissue and *in vitro*. a) DDC-SEM of a large calcification within a human carotid artery plaque section. (scale = 2 μm) b) Magnified image of large calcification using DDC-SEM. (scale = 500 nm) c) DDC-SEM of calcifying EVs within a synthetic collagen hydrogel. (scale = 500 nm) d) Confocal reflection optical section of an aggregate structure observed between collagen fibers (yellow arrow) in a collagen hydrogel with calcification stained by a near-infrared calcium tracer (insert) within aggregate structure. (scale = 2 μm) e) Super-resolution structure illumination microscopy of aggregate of individual fluorescently labeled EVs (arrow). f) Near-infrared calcium tracer signal (arrow) observed using super-resolution structure illumination microscopy of fluorescently labeled EV aggregate. g) EV fluorescence and near-infrared calcium tracer overlay from super-resolution structure illumination microscopy images (scale = 500 nm). h) Aggregation occurred on the surface of the culture well plates in the absence of collagen with an average aggregate volume of 4,567 μm^3. Adding the conditioned media to hydrogels composed of 0.1 mg/ml collagen, led to a 33% reduction in the size of the aggregates formed. Increasing the collagen concentration within the hydrogels to 1 mg/ml further reduced the average aggregate size by 90% compared to the samples without collagen (n = 4 independent experiments, ANOVA, * signifies $p < 0.05$, *** signifies $p < 0.001$). i) Nanoparticle tracking analysis (NTA) histogram of size distribution of EVs incubated at 37 °C for 1 (black line) or 7 days (red line). j) By dividing the objects detected by NTA into 100 nm bins, the mean diameter measured by NTA increased from 156.2±16.4 nm at day 1 to 199.5±27.1 nm at day 5 and 214.7±44.5 nm at day 7. The percentage of aggregates with a diameter larger than 300 nm increased from 4.4±2.4% at day 1 to 14.8±11.9% at day 5 and 22.5±10.6% at day 7. (n = 3 independent experiments). k) Quantification of mineralization of control (black line) and calcifying EVs (red line) incubated for 0, 1, 3, 5, or 7 days. (n = 3 independent experiments, ANOVA, *** signifies $p < 0.001$).

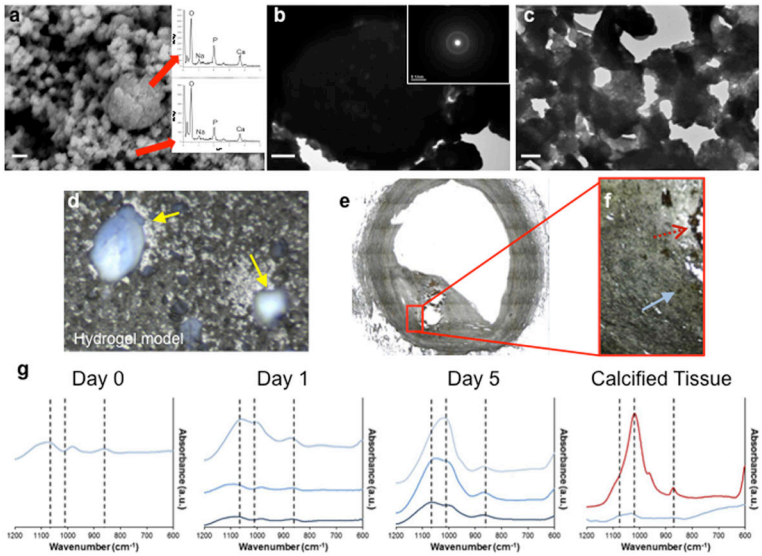

Fig. 4.

EV calcification growth and maturation. a) Energy-dispersive x-ray spectroscopic analyses (EDS, insert) of dense aggregate structures isolated from a synthetic collagen hydrogel identified by SEM. (scale = 500 nm) b, c) TEM images of calcifying structures isolated from synthetic collagen hydrogels with selected-area electron diffraction (d, insert). (scale = 200 nm) d) Identification of calcific mineral for FTIR analysis (yellow arrows) from collagen hydrogels in bright field image. e) Composite bright field image of human carotid atherosclerotic plaque showing scanned FTIR scanned area (box). f) Magnified image of FTIR scanned area of human carotid atherosclerotic plaque with identifiable large calcification regions (red dashed arrow) and microcalcifications (blue arrow). g) FTIR absorbance spectra of mineral from EVs incubated without collagen (lightest blue spectra lines) or with hydrogels of 0.1 mg/ml collagen (medium blue spectra lines) or 1 mg/ml collagen (darkest blue spectra lines), and FTIR absorbance spectra of large calcification (dark red spectrum line) and microcalcification (light blue spectrum line).

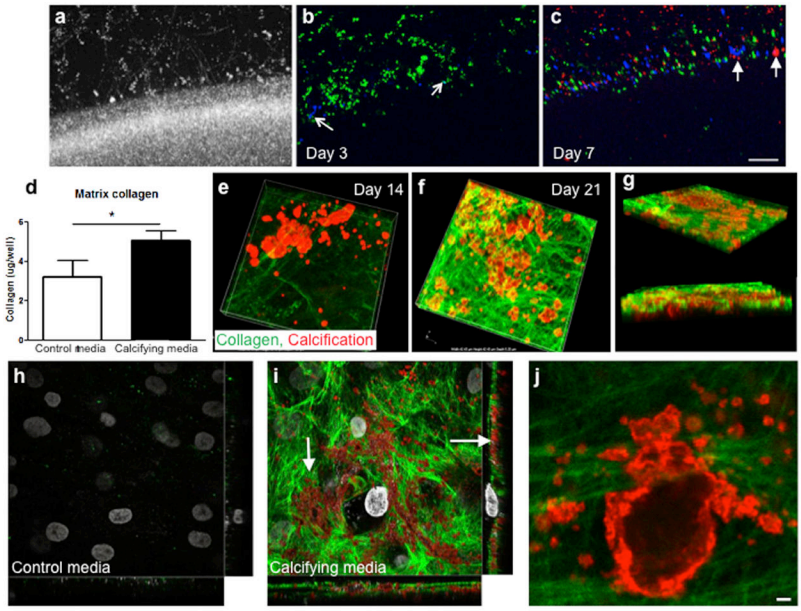

Fig. 5.

Collagen entrapment of calcifying EVs. a) Confocal reflection image of layered hydrogel containing a border between high and low density collagen. b) Confocal fluorescence image of layered hydrogel 3 days following the introduction of green-labeled EVs aggregating with blue-labeled EVs (arrows) added 1 day later. c) Confocal fluorescence image of layered hydrogel 7 days following the addition of green-labeled EVs and 6 days following the addition of blue-labeled EVs. Red fluorescence indicates calcification at border between collagen densities (arrows). d) Picrosirius red colorimetric assay of collagen accumulation in human coronary artery SMCs cultured in control and calcifying media. (n=3, Student's t-test, * signifies $p < 0.05$) e) 3D reconstruction from confocal z-stack images of collagen (green) and calcification (red) in SMCs cultured in calcifying media for 14 days. f) 3D reconstruction from confocal z-stack images of collagen (green) and calcification (red) in SMCs cultured in calcifying media for 21 days. g) Profile view of 21 day 3D reconstruction. h) Image from confocal z-stack image and orthogonal view of all z-stack images of collagen stained with a custom probe (green) and calcification identified by a near-infrared calcium tracer (red) in SMCs cultured in control media for 21 days. i) Image from confocal z-stack image and orthogonal view of all z-stack images of collagen (green) and calcification (red) in SMCs cultured in calcifying media for 21 days. j) Magnified confocal z-stack image of calcification within SMC-produced collagen (scale = 1 μm).

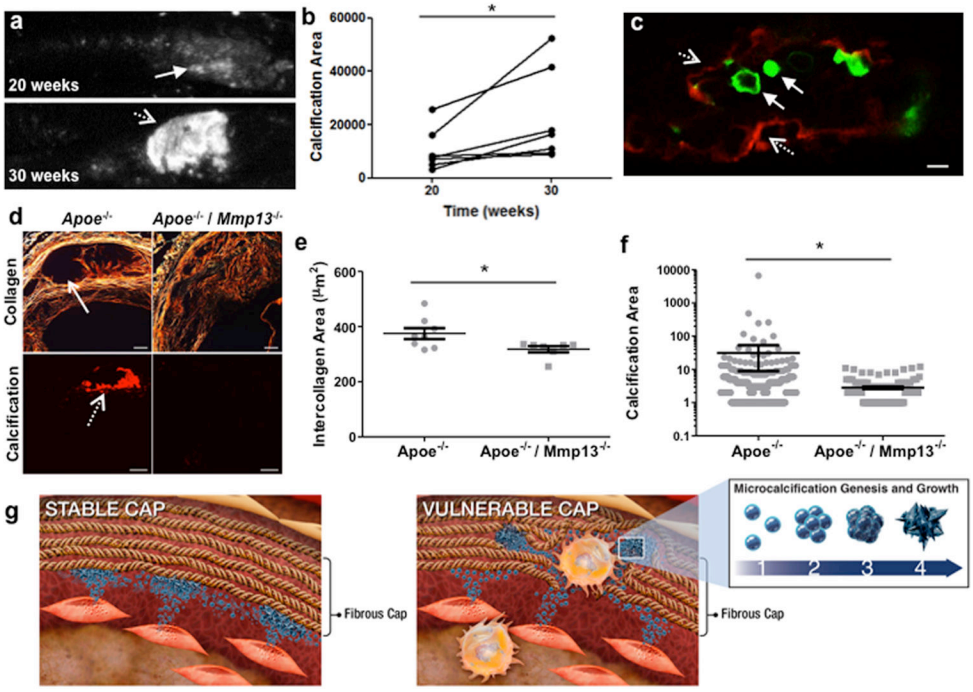

Fig. 6.

In vivo models of calcification growth. a) Intravital imaging of an apoE$^{-/-}$ mouse carotid artery at 20 weeks shows spotty microcalcifications (arrow) that are replaced by large calcification (dashed arrow) at 30 weeks. b) Quantification of calcification area (pixels) in carotid arteries of *Apoe*$^{-/-}$ mice at 20 and 30 weeks measured by intravital microscopy. Lines connect the same artery measured at each time point. (n = 6 different mice, paired t test, * signifies $p < 0.05$) c) Confocal fluorescence image of calcification within an atherosclerotic plaque from a histological section of an *Apoe*$^{-/-}$ mouse. The mouse received an intravenous inject of the fluorescent calcium tracer calcein green at 20 weeks (arrows) followed by an intravenous injection of the fluorescent calcium tracer alizarin red S at 23 weeks (dashed arrow). (scale = 10 μm) d) Representative images of collagen (identified by picrosirius red staining) and calcification (identified by near infrared fluorescence staining) shows large gaps in collagen (arrow) and corresponding large calcification (dashed arrow) in *Apoe*$^{-/-}$ mice. *Apoe*$^{-/-}$/*Mmp13*$^{-/-}$ mice exhibit more dense collagen and no calcification. e) Quantification of average gap area between collagen fibers in *Apoe*$^{-/-}$ and *Apoe*$^{-/-}$/*Mmp13*$^{-/-}$ mice. (n = 8 mice per group, Student's t-test, * signifies $p < 0.05$) f) Quantification of the area of each calcification identified in *Apoe*$^{-/-}$ and *Apoe*$^{-/-}$/*Mmp13*$^{-/-}$ mice. (n = 8 mice per group, Mann-Whitney U test, * signifies $p < 0.05$) g) Schematic of proposed link between collagen content and calcification morphology.